algorithms

MDPI

Article

Stochastic Disruption of Synchronization Patterns in Coupled Non-Identical Neurons

Irina A. Bashkirtseva [1], Lev B. Ryashko [1], Ivan N. Tsvetkov [1] and Alexander N. Pisarchik [2*]

[1] Institute of Mathematics and Computer Science, Ural Federal University, Lenina, 51, Ekaterinburg 620000, Russia; irina.bashkirtseva@urfu.ru (I.A.B.); lev.ryashko@urfu.ru (L.B.R.); itsvet.e1@yandex.ru (I.N.T.)

[2] Centro de Tecnología Biomédica, Universidad Politécnica de Madrid, Campus de Montegancedo, Pozuelo de Alarcón, 28223 Madrid, Spain

* Correspondence: alexander.pisarchik@upm.es

Abstract: We investigate the stochastic disruption of synchronization patterns in a system of two non-identical Rulkov neurons coupled via an electrical synapse. By analyzing the system deterministic dynamics, we identify regions of mono-, bi-, and tristability, corresponding to distinct synchronization regimes as a function of coupling strength. Introducing stochastic perturbations to the coupling parameter, we explore how noise influences synchronization patterns, leading to transitions between different regimes. Notably, we find that increasing noise intensity disrupts lag synchronization, resulting in intermittent switching between a synchronous three-cycle regime and asynchronous chaotic states. This intermittency is closely linked to the structure of chaotic transient basins, and we determine a noise intensity range in which such behavior persists, depending on the coupling strength. Using both numerical simulations and an analytical confidence ellipse method, we provide a comprehensive characterization of these noise-induced effects. Our findings contribute to the understanding of stochastic synchronization phenomena in coupled neuronal systems and offer potential implications for neural dynamics in biological and artificial networks.

Keywords: Rulkov map; neuronal model; coupled neurons; nonlinear dynamics; chaos; noise; intermittency; synchronization

check for updates

Academic Editor: Frank Werner

Received: 8 April 2025
Revised: 13 May 2025
Accepted: 27 May 2025
Published: 30 May 2025

Citation: Bashkirtseva, I.A.; Ryashko, L.B.; Tsvetkov, I.N.; Pisarchik, A.N. Stochastic Disruption of Synchronization Patterns in Coupled Non-Identical Neurons. *Algorithms* **2025**, *18*, 330. https://doi.org/10.3390/a18060330

Copyright: © 2025 by the authors. Licensee MDPI, Basel, Switzerland. This article is an open access article distributed under the terms and conditions of the Creative Commons Attribution (CC BY) license (https://creativecommons.org/licenses/by/4.0/).

1. Introduction

In neuronal networks, synchronization plays a crucial role in information processing, neural coding, and motor control, and its disruption has been implicated in various neurological disorders such as epilepsy, Parkinson's disease, and schizophrenia [1–7]. Real-world neuronal networks are subject to stochastic fluctuations arising from intrinsic neural noise, synaptic variability, and external perturbations [8–11]. These fluctuations can significantly impact neuronal dynamics, leading to intermittent synchronization [12,13], chaotic transitions [14], and complete desynchronization [15,16]. In multistable systems, noise can lead to switching between coexisting attractors, resulting in multistate intermittency and monostability [17–20]. Therefore, studying the stability and stochastic disruption of synchronization in coupled neurons is of great theoretical and practical significance.

In this work, we investigate how random perturbations of the coupling parameter influence synchronization patterns in a coupled neural system. As our neural model, we consider a pair of non-identical Rulkov neurons connected via an electrical synapse [21,22]. The Rulkov model is widely used to represent neuronal bursting dynamics due to its computational efficiency and its ability to capture essential aspects of neuronal excitability.

Both deterministic and stochastic behaviors in isolated Rulkov neurons have been the focus of extensive research [23–27].

The Rulkov map strikes a compelling balance between biological realism and mathematical simplicity, distinguishing it from other discrete-time dynamical systems. Its ability to replicate key neuronal behaviors, such as spiking, bursting, and excitability, within a low-dimensional, discrete-time framework has made it a popular choice in computational neuroscience. This efficiency makes it especially suitable for large-scale simulations of neuronal networks, where computational resources are a limiting factor. Additionally, its structural simplicity allows for in-depth analytical exploration of complex dynamical phenomena, including bifurcations, chaos, multistability, and noise-induced intermittency. These features make the Rulkov map an invaluable tool for both theoretical studies in nonlinear dynamics and practical modeling of large neuronal systems.

Coupled Rulkov neurons exhibit rich dynamical behaviors, including multiple synchronization regimes that depend on the coupling strength and system parameters [28–30]. Depending on the coupling parameter, different dynamical regimes (mono-, bi-, and tristable) and synchronous states, such as in-phase and lag synchronization, can emerge. While previous studies have focused primarily on noise-induced effects in networks of chaotic neurons exhibiting bursting dynamics, our work, to the best of our knowledge, is the first to investigate the impact of stochastic perturbations in a system of coupled regular, non-chaotic neurons that display stable three-cycles in the isolated state. This allows us to explore a previously underexamined regime where noise induces transitions from multistable lag synchronization to monostable in-phase synchronization, as well as intermittent desynchronization via noise-driven chaotic bursts.

Through systematic parametric analysis, we identify key conditions under which noise intensity influences the transitions between different dynamical states. To analyze these complex dynamics, we employ a combination of direct numerical simulations and an analytical method based on confidence domains, which provide a robust statistical tool for assessing the variability of system trajectories under stochastic perturbations, allowing us to characterize the range of noise intensity that sustains intermittency and determine its dependence on coupling strength. The size and shape of the confidence domains are determined from the stochastic sensitivity matrices of the corresponding deterministic attractors. The stochastic sensitivity function technique was elaborated for different types of regular and chaotic attractors [31] and is now actively used in the parametric analysis of various stochastic phenomena (see, e.g., [32–37]).

A particularly intriguing phenomenon observed in our study is the existence of an intermittency regime, where a synchronous three-cycle regime is interrupted by asynchronous chaotic bursts. This phenomenon underscores the critical role of basins of chaotic transients in shaping the response of the system to stochastic perturbations. The presence of intermittent chaotic behavior suggests that noise can induce transitions between metastable states, highlighting the nontrivial interplay between deterministic and stochastic influences in coupled neuronal dynamics. In this paper, we extend previous research by systematically characterizing noise-induced intermittency and synchronization in a parameter region where the system exhibits coexisting regimes, an aspect less explored in the literature. We focus on a new and complementary question: how the joint dynamics evolves with respect to variations in the coupling strength and noise intensity. We explore the combined effects of weak heterogeneity and stochasticity, which are both relevant to real neuronal systems.

The rest of this paper is organized as follows: Section 2 introduces the deterministic model of coupled Rulkov neurons and explores their dynamical behavior. Section 3 extends the discussion to the stochastic model, highlighting synchronization regimes and scenarios of stochastic disruption. In Section 4, we analyze intermittent chaotic behavior in

detail. Finally, Section 5 summarizes our findings and discusses potential directions for future research.

2. Deterministic Model

Consider a system of two non-identical neurons modeled by the Rulkov map [21] and mutually coupled by electrical synapses:

$$\begin{aligned} x_{t+1} &= f(\gamma_1, x_t) + \sigma(y_t - x_t), \\ y_{t+1} &= f(\gamma_2, y_t) + \sigma(x_t - y_t). \end{aligned} \tag{1}$$

Here, $f(\gamma, u) = \frac{\alpha}{1+u^2} + \gamma$, $\alpha = 4.1$. In system (1), $\gamma_2 = \gamma_1 + \Delta$, where Δ is a mismatch parameter. The parameter σ is the coupling strength. The parameter ranges explored in our study are consistent with those established in Rulkov's original work [21] and widely adopted in subsequent studies [24,25,27–30]. This choice ensures comparability with existing results and situates our analysis within a well-studied regime of the model that is known to exhibit rich dynamical behavior, including multistability and noise-induced transitions.

2.1. Dynamics of Isolated Neuron

Figure 1 shows the γ-interval in which the isolated neuron $x_{t+1} = \frac{\alpha}{1+x_t^2} + \gamma$ demonstrates the transformation of a stable three-cycle into a chaotic attractor when γ passes the crisis bifurcation point $\gamma_{cr} = -1.74722$. This transition from order to chaos is justified by the largest Lyapunov exponent Λ in the bottom panel.

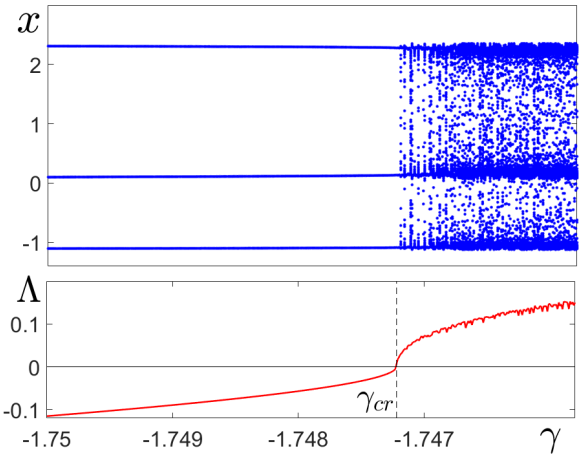


Figure 1. Bifurcation diagram (blue) and Lyapunov exponent (red) of the isolated Rulkov system. The crisis bifurcation occurs at $\gamma_{cr} = -1.74722$.

2.2. Dynamics of Coupled Neurons

Now, consider the cooperative dynamics of the coupled system (1) with $\gamma_1 = -1.75$ and $\gamma_2 = -1.748$; i.e., the neurons are non-identical with a parameter mismatch of $\Delta = 0.002$. The influence of non-identity in coupled deterministic Rulkov neurons has been previously analyzed in detail in our recent paper [38] for $\gamma = -1.75$, where we compared the dynamics for identical neurons ($\Delta = 0$) and slightly non-identical ones ($\Delta \in (0, 0.002)$) under varying coupling strength σ. Our findings showed that although the overall qualitative behavior remains similar—i.e., transitions between ordered and chaotic regimes with increasing σ—the precise thresholds shift with increasing non-identity. Specifically, a larger Δ tends to lower the critical value of σ at which the transition from regular to chaotic behavior occurs.

While isolated neurons with these parameters exhibit three-cycles, the joint dynamics is governed by the coupling parameter σ, as illustrated in Figure 2, which presents the bifurcation diagram of the x variable.

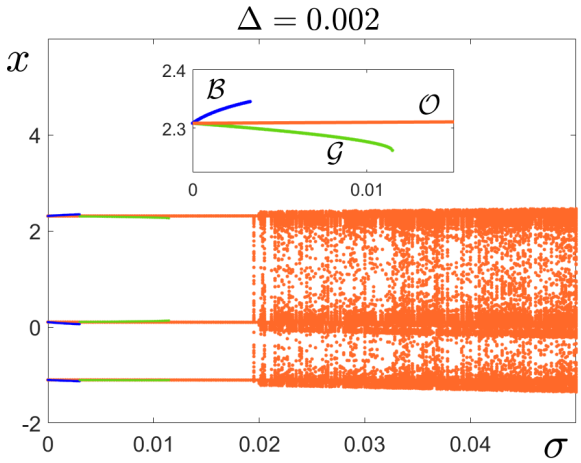


Figure 2. Bifurcation diagram of system (1) with $\gamma_1 = -1.75$ and $\Delta = 0.002$. Here, the x-coordinates of the coexisting 3-cycles $\mathcal{B}$, $\mathcal{G}$, and $\mathcal{O}$ are shown in blue, green, and orange, respectively. In the insert, we plot the enlarged fragment at small σ.

At weak coupling strengths, system (1) exhibits tristability, with three coexisting three-cycles: $\mathcal{B}$ (blue), $\mathcal{G}$ (green), and $\mathcal{O}$ (orange). These attractors and their basins of attraction are illustrated in Figure 3 for different values of the coupling parameter σ. To compute the basins of attraction, we used a uniform grid of 300×300 initial conditions in the (x, y) plane. Each point on the grid was integrated using system (1) for 1000 iterations. A trajectory was considered to belong to a given attractor if it converged to that attractor with a numerical tolerance of 0.001, based on the Euclidean distance between the final iterates and the attractor's orbit.

Figure 3a illustrates the coexistence of three three-cycles at $\sigma = 0.003$. As the coupling increases, cycle $\mathcal{B}$ is annihilated, reducing system (1) to a bistable state with two coexisting three-cycles, $\mathcal{G}$ and $\mathcal{O}$, at $\sigma = 0.01$ (Figure 3b). A further increase in σ eliminates cycle $\mathcal{G}$, making the system monostable with a single remaining attractor, cycle $\mathcal{O}$, at $\sigma = 0.015$ (Figure 3c). Finally, at the crisis bifurcation occurring at $\sigma_* = 0.019011$, cycle $\mathcal{O}$ loses stability, causing the system to transition into chaos. The resulting chaotic attractor is shown in Figure 3d for $\sigma = 0.05$.

The cycles $\mathcal{B}$, $\mathcal{G}$, and $\mathcal{O}$ correspond to different synchronization patterns. Solutions originating from the basins of $\mathcal{B}$ and $\mathcal{G}$ exhibit synchronization in a one-step shift mode. In the basin of $\mathcal{B}$, solutions stabilize to a three-cycle where the y-coordinate is one step ahead of the x-coordinate, which we denote as the $[-]$ synchronization mode. Conversely, in the basin of $\mathcal{G}$, solutions stabilize to a three-cycle for which the y-coordinate lags one step behind the x-coordinate, referred to as the $[+]$ synchronization mode. Finally, solutions in the basin of $\mathcal{O}$ stabilize to a three-cycle without any coordinate shift, denoted as the $[0]$ synchronization mode. Thus, as the coupling increases, the system first loses the $[-]$ synchronization mode, followed by the $[+]$ synchronization mode.

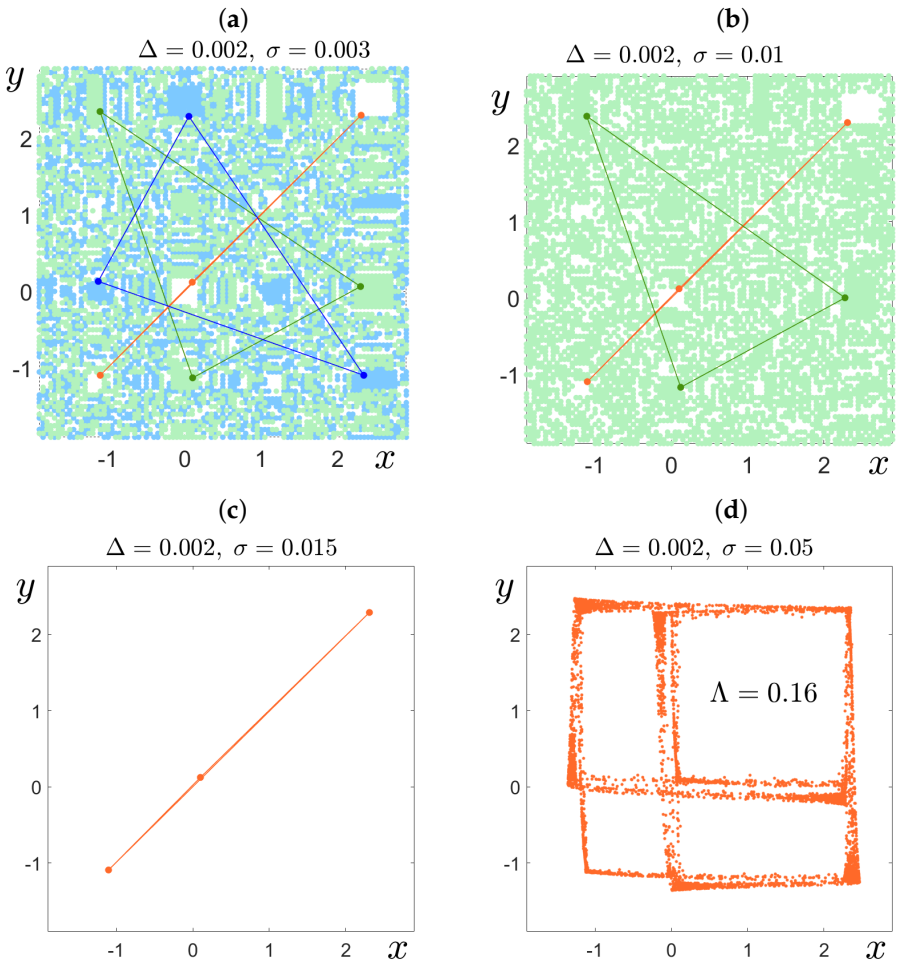


Figure 3. Attractors and their basins of attraction of system (1) with $\gamma_1 = -1.75$ and $\Delta = 0.002$ at coupling strengths: (**a**) $\sigma = 0.003$, tristability with coexisting 3-cycles $\mathcal{B}$, $\mathcal{G}$, and $\mathcal{O}$ shown in blue, green, and orange; (**b**) $\sigma = 0.01$, bistability with coexisting 3-cycles $\mathcal{G}$ and $\mathcal{O}$ shown in green and orange; (**c**) $\sigma = 0.02$, monostability with the 3-cycle $\mathcal{O}$ shown in orange; and (**d**) $\sigma = 0.05$, monostability with the chaotic attractor (orange) having positive Lyapunov exponent $\Lambda = 0.16$.

3. Stochastic Model

Let us now study how noise influences system (1). The dynamics of the coupled neurons under random fluctuations in the coupling parameter, $\sigma : \sigma \to \sigma + \varepsilon\xi_t$, is governed by the following equations:

$$\begin{aligned} x_{t+1} &= f(\gamma_1, x_t) + (\sigma + \varepsilon\xi_t)(y_t - x_t), \\ y_{t+1} &= f(\gamma_2, y_t) + (\sigma + \varepsilon\xi_t)(x_t - y_t). \end{aligned} \tag{2}$$

Here, ξ_t represents uncorrelated white Gaussian noise with intensity ε.

Next, we analyze how the solutions of system (2) depend on the noise intensity ε.

3.1. Stochastic Deformations in the Tristability Case

First, consider system (2) with $\sigma = 0.003$. As shown in the previous section, at this coupling strength, the deterministic system (1) exhibits the coexistence of three three-cycles ($\mathcal{O}$, $\mathcal{B}$, and $\mathcal{G}$), as illustrated in Figure 3a.

Figure 4 demonstrates how stochastic perturbations in the coupling parameter influence the system dynamics. In Figure 4a–c, we plot the evolution of the difference between the x- and y-coordinates ($x - y$) of solutions corresponding to cycles $\mathcal{O}$ (orange), $\mathcal{G}$ (green), and $\mathcal{B}$ (blue) under three different noise intensities.

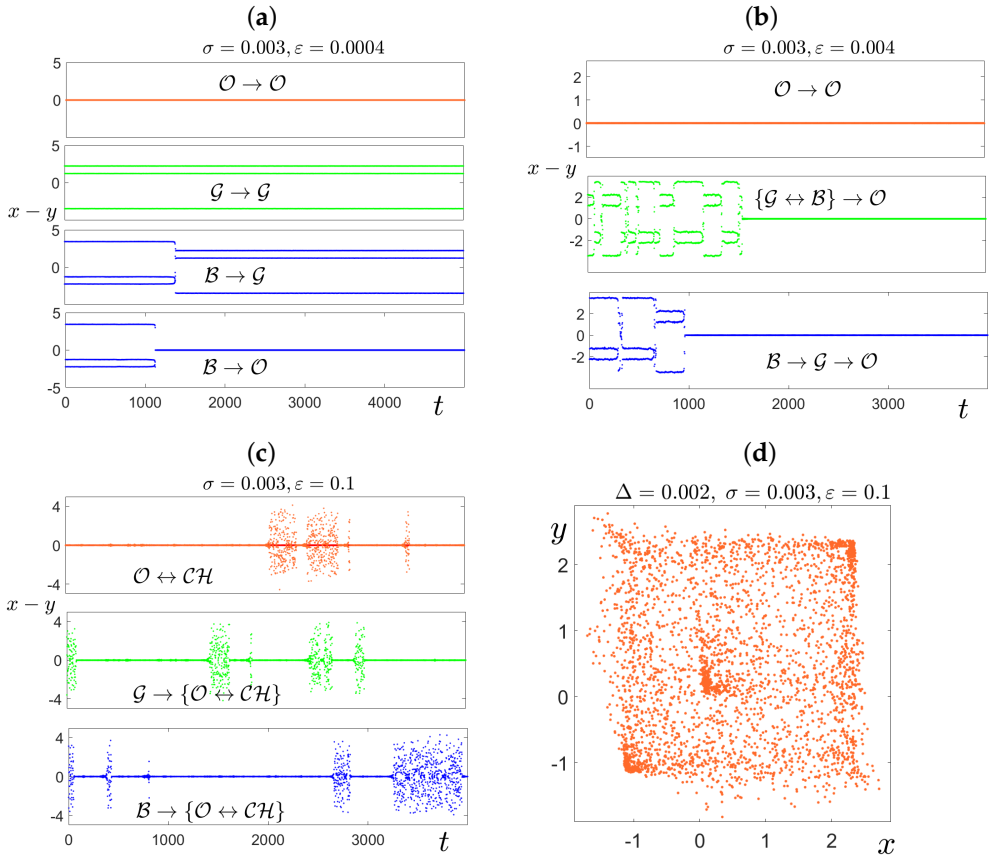


Figure 4. Time series of the $(x - y)$ coordinate in the tristable system (2) with $\gamma = -1.75, \Delta = 0.002$, and $\sigma = 0.003$, starting from cycles $\mathcal{O}$ (orange), $\mathcal{G}$ (green), and cycle $\mathcal{B}$ (blue) under different noise intensities: (**a**) $\varepsilon = 0.0004$, (**b**) $\varepsilon = 0.004$, and (**c**) $\varepsilon = 0.1$. The arrows indicate the directions of transitions between coexisting 3-cycles. (**d**) Random states of system (2) with $\varepsilon = 0.1$.

For weak noise ($\varepsilon = 0.0004$), stochastic solutions of system (2) that start at cycles $\mathcal{O}$ or $\mathcal{G}$ remain in these cycles, as shown in the upper two panels of Figure 4a. However, the trajectories that begin at cycle $\mathcal{B}$ eventually switch to either cycle $\mathcal{G}$ or $\mathcal{O}$ after a transient period, as illustrated in the lower two panels. Thus, weak noise disrupts cycle $\mathcal{B}$ while leaving the other cycles unaffected.

As shown in Figure 4b, stronger noise ($\varepsilon = 0.004$) not only eliminates cycle $\mathcal{B}$ (lowest panel) but also destroys cycle $\mathcal{G}$ (middle panel) while cycle $\mathcal{O}$ remains unaffected (upper panel). Interestingly, solutions that start at $\mathcal{G}$ (middle panel) exhibit mutual transitions between $\mathcal{G}$ and $\mathcal{B}$ ($\mathcal{G} \leftrightarrow \mathcal{B}$), eventually stabilizing near cycle $\mathcal{O}$. Meanwhile, solutions originating from $\mathcal{B}$ undergo sequential transitions $\mathcal{B} \to \mathcal{G} \to \mathcal{O}$. Thus, regardless of the initial conditions, all transitions at this noise level ultimately lead to cycle $\mathcal{O}$, making the system monostable.

When the noise intensity increases to $\varepsilon = 0.1$, all three cycles lose stability. At this noise level, each cycle is disrupted by chaotic bursts, as shown in Figure 4c. The system undergoes the following stochastic transitions: $\mathcal{O} \leftrightarrow \mathcal{CH}$, $\mathcal{G} \to \mathcal{O} \leftrightarrow \mathcal{CH}$, and $\mathcal{B} \to \mathcal{O} \leftrightarrow \mathcal{CH}$. Thus, regardless of the initial state, the stochastic system (2) transitions into an intermittent regime characterized by alternating small-amplitude stochastic oscillations near $\mathcal{O}$ and large-amplitude chaotic oscillations $\mathcal{CH}$. Random states of this chaotic regime are depicted in Figure 4d.

Figure 5 illustrates the stochastic transformations of the $(x - y)$ variable as the noise intensity ε gradually increases, starting from deterministic cycles $\mathcal{B}$ (Figure 5a), $\mathcal{G}$ (Figure 5b), and $\mathcal{O}$ (Figure 5c). These cycles are shown in the background in light colors. Colored dots

represent 100 successive random states of system (2) for solutions initiated at cycles $\mathcal{B}$, $\mathcal{G}$, and $\mathcal{O}$, plotted after 1000 transient steps. The color of these dots matches the corresponding starting cycle but appears in a brighter shade.

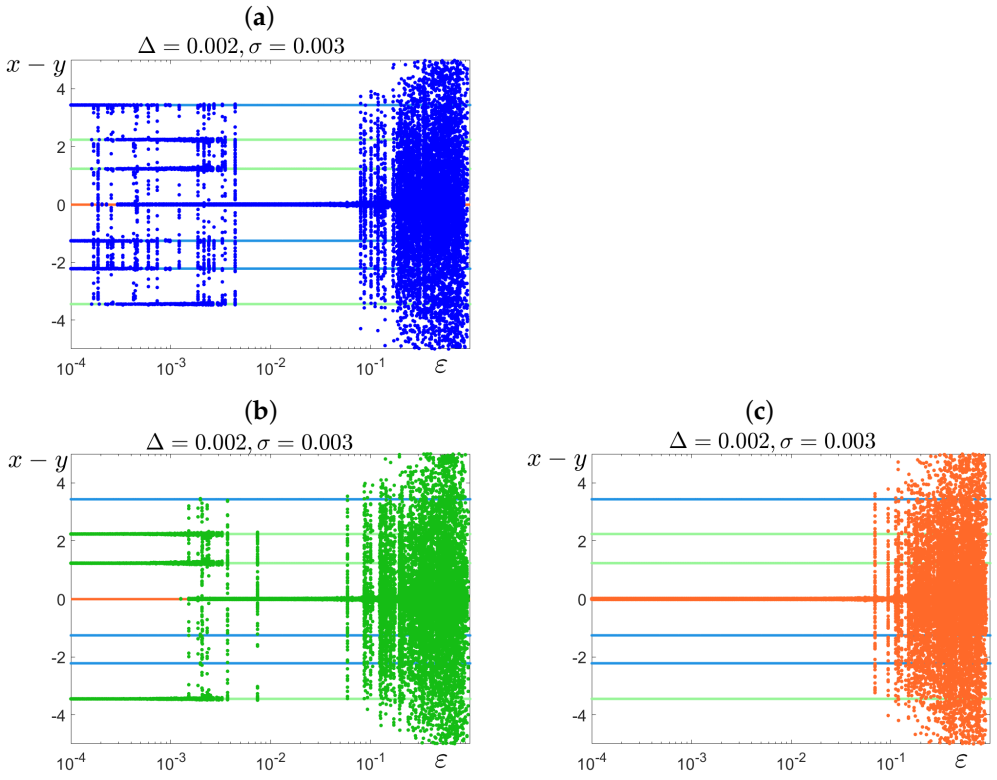


Figure 5. Stochastic transitions in the $(x - y)$ variable of solutions for the tristable system (2) with $\gamma = -1.75, \Delta = 0.002$, and $\sigma = 0.003$ as a function of noise intensity ε, starting from (**a**) cycle $\mathcal{B}$ (blue), (**b**) cycle $\mathcal{G}$ (green), and (**c**) cycle $\mathcal{O}$ (orange). The deterministic cycles are shown in the background by the corresponding light colors.

For weak noise, the random solutions remain close to their respective starting cycles. However, as the noise intensity increases, stochastic switches between coexisting states begin to appear, as shown in the time series in Figure 4a,b. These transitions are revealed in Figure 5 as dots between horizontal lines.

In the case of $\mathcal{B}$ (Figure 5a), these transitions disrupt the $[-]$ synchronization mode. As the noise intensity increases further, random states begin clustering around cycle $\mathcal{O}$ (see the time series in Figure 4b). This indicates that both the $[-]$ and $[+]$ synchronization modes are destroyed, leaving only the $[0]$ synchronization mode intact. When the noise becomes sufficiently strong, solutions starting at $\mathcal{B}$ transition directly into the intermittent regime $\mathcal{O} \leftrightarrow \mathcal{CH}$, characterized by alternating small-amplitude stochastic oscillations near $\mathcal{O}$ and large-amplitude chaotic oscillations near $\mathcal{CH}$ (see the time series and random states in Figure 4c,d). Consequently, the $[0]$ synchronization mode is temporarily disrupted by random disturbances.

Stochastic transformations of solutions starting from the three-cycle $\mathcal{G}$ are shown in Figure 5b. For noise intensities up to $\varepsilon = 10^{-3}$, these solutions remain localized near the deterministic cycle. At $\varepsilon = 0.004$, stochastic transformations following the sequence $\{\mathcal{G} \leftrightarrow \mathcal{B}\} \rightarrow \mathcal{O}$ are observed, as illustrated in the time series in Figure 4b (green trace). For stronger noise, the stochastic system transits to the regime $\mathcal{G} \rightarrow \{\mathcal{O} \leftrightarrow \mathcal{CH}\}$ (see the time series shown in green in Figure 4c for $\varepsilon = 0.1$). For solutions starting at the three-cycle $\mathcal{O}$, only a single-stage stochastic transformation occurs, where noisy oscillations near $\mathcal{O}$ transition into the intermittent mode $\mathcal{O} \leftrightarrow \mathcal{CH}$ (see the orange time series in Figure 4c for $\varepsilon = 0.1$).

To summarize the effect of noise in the tristability case, increasing noise intensity first destroys cycle $\mathcal{B}$, followed by the destruction of cycle $\mathcal{G}$, leaving cycle $\mathcal{O}$ as the most resilient to noise.

3.2. Confidence Domain Method

The cycle breakdown process described above can be analyzed analytically using the confidence domain method [31], where the mutual arrangement of confidence domains and attractors' basins of attraction plays a key role. Below, we briefly present details of the confidence domain method.

Consider a deterministic system with an exponentially stable three-cycle consisting of successive states $(\bar{x}_1, \bar{y}_1)$, $(\bar{x}_2, \bar{y}_2)$, and $(\bar{x}_3, \bar{y}_3)$. Under random disturbances, the stochastic sensitivity of these states is determined by the corresponding matrices W_1, W_2, and W_3. These matrices satisfy the following algebraic equations (see mathematical details in [31]):

$$W_2 = F_1 W_1 F_1^\top + Q_1, \quad W_3 = F_2 W_2 F_2^\top + Q_2, \quad W_1 = F_3 W_3 F_3^\top + Q_3.$$

Here, F_t is the Jacobi matrix at the point $(\bar{x}_t, \bar{y}_t)$ of the three-cycle, while the matrices Q_t characterize the stochastic disturbances.

For system (2), the matrix Q_t is given by

$$Q_t = (\bar{y}_t - \bar{x}_t)^2 \begin{bmatrix} 1 & -1 \\ -1 & 1 \end{bmatrix}.$$

The stochastic sensitivity matrix W_1 satisfies the matrix equation

$$W_1 = F W_1 F^\top + Q,$$

where $F = F_3 F_2 F_1$, $\quad Q = Q_3 + F_3 Q_2 F_3^\top + F_3 F_2 Q_1 F_2^\top F_3^\top$. The other stochastic sensitivity matrices, W_2 and W_3, can be determined using the recurrence relations provided earlier.

These stochastic sensitivity matrices are useful for approximating the dispersion of random states around the points of the deterministic three-cycle. Let $\rho_t(x, y)$ be the stationary probability density distribution of stochastic solutions near the state $(\bar{x}_t, \bar{y}_t)$ of the deterministic cycle. Then, the Gaussian approximation of the function $\rho_t(x, y)$ is written as

$$\rho_t(x, y) \approx K \exp\left[\frac{1}{2\varepsilon^2} \begin{pmatrix} x - \bar{x}_t \\ y - \bar{y}_t \end{pmatrix}^\top W_t^{-1} \begin{pmatrix} x - \bar{x}_t \\ y - \bar{y}_t \end{pmatrix}\right]. \tag{3}$$

So, the stochastic sensitivity matrices W_t play a key role in describing the dispersion of random states near points of the deterministic cycle.

The approximations (3) can be used to geometrically characterize the distribution of random states in the form of confidence ellipses. For each state $(\bar{x}_t, \bar{y}_t)$ of the three-cycle, the confidence ellipse is defined as

$$\frac{\alpha_1^2}{\mu_{1,t}} + \frac{\alpha_2^2}{\mu_{2,t}} = -2\varepsilon^2 \ln(1 - P), \qquad (t = 1, 2, 3).$$

Here, α_1 and α_2 are the coordinates of the ellipse in the basis of normalized eigenvectors $u_{1,t}$ and $u_{2,t}$ of the matrix W_t, while $\mu_{1,t}$ and $\mu_{2,t}$ are the corresponding eigenvalues. The parameter P represents the fiducial probability.

In Figure 6, we present magnified fragments of the phase plane of the deterministic system (1), highlighting the basins of attraction near specific states of the three-cycles. The basin points are color-coded: light blue for cycle $\mathcal{B}$, light green for cycle $\mathcal{G}$, and white for

cycle $\mathcal{O}$. A notable feature of these basins is the distinction between solid and fractal parts. The solid region surrounds the cycle points, while outside this area, the basins of all three three-cycles are fractally interwoven.

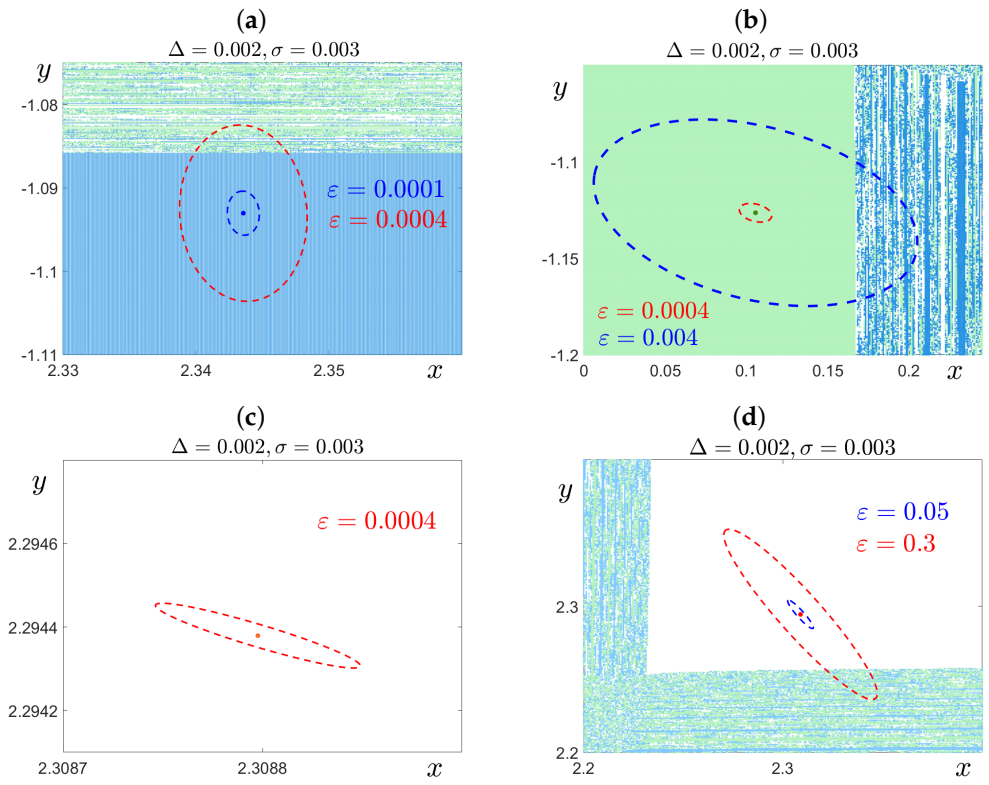


Figure 6. Illustration of the confidence domain method in the stochastic system (2) with $\gamma = -1.75$, $\Delta = 0.002$, and $\sigma = 0.003$. Enlarged fragments of the phase plane of the deterministic system (1) show the solid and fractional parts of basins for cycle $\mathcal{B}$ (light blue), cycle $\mathcal{G}$ (light green), and cycle $\mathcal{O}$ (white), along with confidence ellipses: (**a**) around the state $(2.3436, -1.0939)$ of cycle $\mathcal{B}$ for $\varepsilon = 0.0001$ (blue) and $\varepsilon = 0.0004$ (red); (**b**) around the state $(0.1056, -1.1264)$ of cycle $\mathcal{G}$ for $\varepsilon = 0.0004$; (**c**) around the state $(2.3088, 2.2944)$ of cycle $\mathcal{O}$ for $\varepsilon = 0.0004$; and (**d**) around the state $(2.3088, 2.2944)$ of cycle $\mathcal{O}$ for $\varepsilon = 0.05$ (blue) and $\varepsilon = 0.3$ (red).

In addition to these deterministic basins, Figure 6 also displays confidence ellipses for the stochastic system (2). As the noise intensity increases, these ellipses expand in size. As long as a confidence ellipse remains within the solid region of a basin, no transitions occur. However, once the ellipse extends beyond the solid part and overlaps with the fractal region, it begins to encompass points from the basins of other coexisting attractors. This expansion marks the breakdown of the initial oscillatory regime and signals transitions to alternative oscillatory modes.

Now, let us examine how the confidence domain method applies in the case of tristability.

In Figure 6a, confidence ellipses are plotted around a point of cycle $\mathcal{B}$ for two noise intensities: $\varepsilon = 0.0001$ and $\varepsilon = 0.0004$. For $\varepsilon = 0.0001$, the ellipse remains entirely within the solid region of the basin, preventing any noise-induced transitions. However, at $\varepsilon = 0.0004$, the ellipse extends into the fractal region of the basin, leading to the stochastic destruction of oscillations near $\mathcal{B}$.

A different scenario is observed near cycle $\mathcal{G}$, where noise with $\varepsilon = 0.0004$ is insufficient to disrupt stochastic oscillations. As shown in Figure 6b, the confidence ellipse remains fully contained within the solid part of the $\mathcal{G}$ basin, ensuring stability. The same holds for cycle $\mathcal{O}$, as depicted in Figure 6c. Consequently, a higher noise intensity is required

to destabilize cycle $\mathcal{G}$. This effect is evident in Figure 6b, where the confidence ellipse for $\varepsilon = 0.004$ extends into the fractal region, signaling the onset of stochastic destruction.

For cycle $\mathcal{O}$, it remains stable even under stronger noise with $\varepsilon = 0.05$ (see blue confidence ellipse in Figure 6d). However, as shown in Figure 6d, when the noise intensity increases to $\varepsilon = 0.3$, the confidence ellipse extends into the fractal part of the basin, indicating the breakdown of noisy oscillations near $\mathcal{O}$.

Notably, the confidence ellipse method predicts that solutions starting from $\mathcal{B}$ and $\mathcal{G}$ transition to $\mathcal{O}$ at $\varepsilon = 0.004$ (see Figure 6a,b). In contrast, the solutions originating from $\mathcal{O}$ remain near $\mathcal{O}$ even up to $\varepsilon = 0.05$ (see Figure 6d). This reveals a broad range of noise intensity, or an "ε-window", where all solutions of the stochastic system (2) reside near $\mathcal{O}$. This finding is supported by the results of numerical simulations presented in Figure 5. Within this ε-window, regardless of the initial conditions, the $[0]$ synchronization mode persists.

It is worth noting that the predictions made using the confidence ellipse method align well with the results of direct numerical simulations discussed in Section 3.1.

3.3. Stochastic Deformations in the Bistability Case

We now consider system (2) with $\sigma = 0.01$, which exhibits bistability in the absence of noise, characterized by the coexistence of three-cycles $\mathcal{O}$ and $\mathcal{G}$ (see Figure 3b). Possible scenarios of noise-induced transformations in the distribution of random states are shown in Figure 7a,b. In Figure 7a, random states of solutions originating from cycle $\mathcal{G}$ are shown as a function of noise intensity ε. A clear transition sequence, $\mathcal{G} \to \mathcal{O} \to \mathcal{CH}$, is observed, indicating the progressive destabilization of the initial cycle as noise increases.

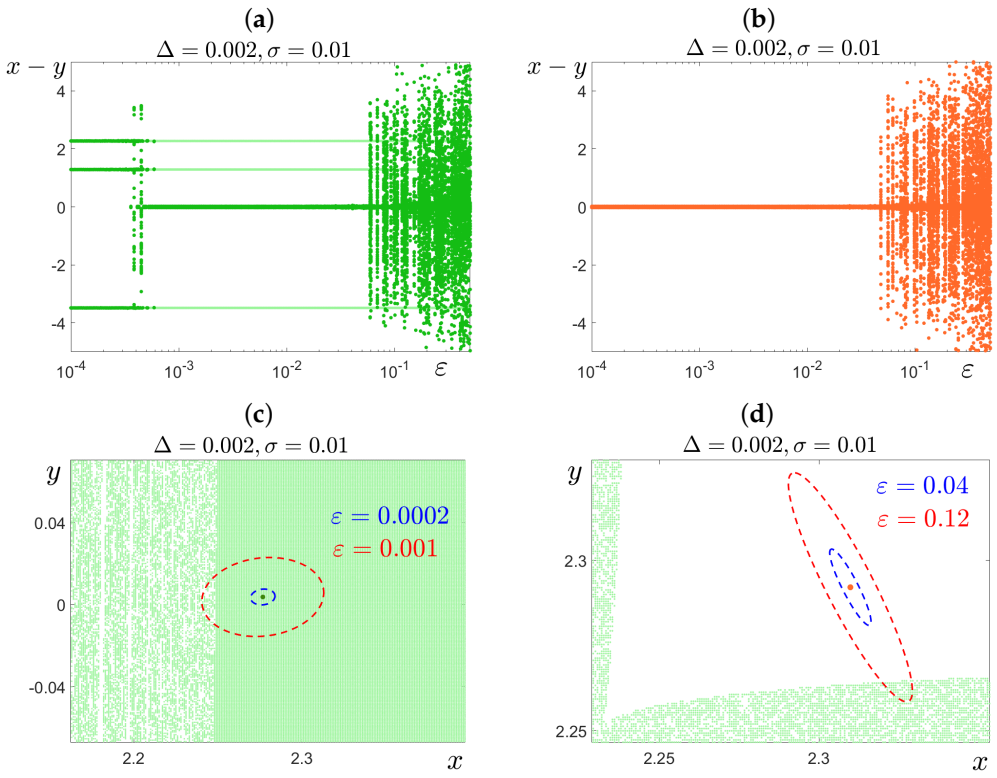


Figure 7. Stochastic transitions in the bistable system (2) with $\gamma = -1.75$, $\Delta = 0.002$, and $\sigma = 0.01$. (**a**) Random states of solutions originating from cycle $\mathcal{G}$ (green) under varying noise intensity ε. (**b**) Random states of solutions originating from cycle $\mathcal{O}$ (orange). (**c**) Enlarged fragment of the phase plane showing confidence ellipses around a state of cycle $\mathcal{G}$ for $\varepsilon = 0.0002$ (blue) and $\varepsilon = 0.001$ (red). (**d**) Enlarged fragment with confidence ellipses around the state of cycle $\mathcal{O}$ for $\varepsilon = 0.04$ (blue) and $\varepsilon = 0.12$ (red). In (**c**,**d**), basins of the cycle $\mathcal{G}$ and $\mathcal{O}$ are shown in green and white, respectively.

The mutual arrangement of basins and confidence ellipses for $\varepsilon = 0.0002$ (blue) and $\varepsilon = 0.001$ (red) is illustrated in Figure 7c. For $\varepsilon = 0.0002$, the confidence ellipse lies entirely within the solid part of the basin of $\mathcal{G}$, meaning that random solutions exhibit only slight fluctuations around $\mathcal{G}$. However, for $\varepsilon = 0.001$, the ellipse extends into the fractal region of the basin, allowing for noise-induced transitions $\mathcal{G} \to \mathcal{O}$. The subsequent transition $\mathcal{O} \to \mathcal{CH}$, observed in Figure 7a,b, is accurately predicted by the confidence ellipses shown in Figure 7d.

3.4. Stochastic Deformations in the Monostability Case

Let us now examine the behavior of the stochastic system (2) in the case of monostability, when the original deterministic system (1) possesses only one attractor: the in-phase three-cycle $\mathcal{O}$. This cycle, corresponding to $\sigma = 0.015$, is shown in Figure 3c. For this parameter value, the evolution of random states originating from $\mathcal{O}$ is presented in Figure 8a as a function of noise intensity ε.

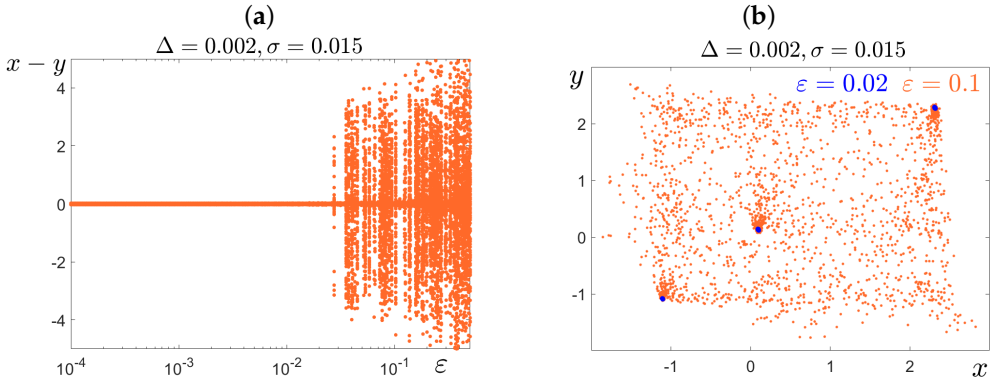


Figure 8. Noise-induced excitation in the monostable system (2) with parameters $\gamma = -1.75$, $\Delta = 0.002$, and $\sigma = 0.015$: (**a**) random states for solutions initiated at cycle $\mathcal{O}$ (orange) versus noise intensity ε; (**b**) phase space representation of random states for $\varepsilon = 0.02$ (blue), showing localization near cycle $\mathcal{O}$, and for $\varepsilon = 0.1$ (orange), illustrating widespread dispersion due to noise-induced excitation.

As evident from the figure, the three-cycle $\mathcal{O}$ demonstrates notable resilience to noise. However, beyond a certain threshold intensity of ε, system (2) undergoes an abrupt change in the probability distribution of its states. Specifically, in Figure 8b, the random states for $\varepsilon = 0.02$ (blue) remain tightly clustered near the deterministic cycle $\mathcal{O}$, whereas for $\varepsilon = 0.1$ (orange), the states are broadly scattered across the phase space. This behavior reflects a clear manifestation of noise-induced excitation. Here, we can note the similarity in the distribution of random states (orange dots) in Figure 4d and Figure 8b for the same $\varepsilon = 0.1$. However, we should emphasize different mechanisms of formation of these distributions. In Figure 4d, for $\sigma = 0.003$, this distribution arises from stochastic transitions between three coexisting cycles, while in Figure 8b, for $\sigma = 0.015$, when the system is monostable, a similar distribution is formed due to the presence of deterministic transients and, as a consequence, stochastic excitability.

To summarize, while in the cases of multistability, sharp deformations in the distributions were attributed to noise-induced transitions between coexisting attractors, the mechanism driving the transformation in this monostable case is different. Here, the influence of transient attractors in the underlying deterministic system (1) becomes significant.

4. Transients And Intermittent Synchronization

In this section, we investigate the transient dynamics of the deterministic system (1) and explore noise-induced intermittent synchronization in the corresponding stochastic system (2).

4.1. Basins of Short and Long Transients

Although the monostable system (1) with $\sigma = 0.015$ ensures that all trajectories eventually converge to the three-cycle $\mathcal{O}$, the rate of convergence strongly depends on the initial conditions. This behavior is illustrated in Figure 9a, where initial points of solutions that take more than 200 iterations to converge to $\mathcal{O}$ with an accuracy of 0.001 are marked in orange. These points define the long-transient basin (LTB), while the remaining region, corresponding to faster convergence, is marked in white and referred to as the short-transient basin (STB). Notably, the boundary between these basins exhibits a complex, fractal structure. In Figure 9b, an enlarged fragment of the phase plane is shown near one of the points of three-cycle $\mathcal{O}$, highlighting both the STB and LTB. The STB consists of a solid (white) region and a fractal part, represented by a mixture of white and orange areas. The selected three-cycle point lies within the solid part of the STB.

We now examine how the transient behavior of solutions to the deterministic system (1) depends on the choice of the initial condition. Specifically, we consider two nearby points, $A(2.32, 2.28)$ and $B(2.32, 2.27)$. Point A lies within the solid part of the STB, whereas point B belongs to its fractal region.

During transients, the system may alternate between synchronous ($x = y$) and asynchronous ($x \neq y$) states. To quantify these states, we introduce the synchronization index defined as

$$z_t = \mathrm{sgn}[(x_{t+1} - x_t)(y_{t+1} - y_t)].$$

Note that $z_t = 1$ when the neurons evolve synchronously (i.e., both variables increase or decrease together), and $z_t = -1$ otherwise. Examples of synchronous and asynchronous transients are shown in Figures 9c and 9d, respectively. Specifically, Figure 9c illustrates that the trajectory starting at point A converges to the three-cycle $\mathcal{O}$ while maintaining in-phase synchronization ($z_t = 1$). In contrast, Figure 9d shows that the trajectory from point B exhibits a large-amplitude burst with temporary desynchronization, characterized by the interval where $z_t = -1$.

The diversity of transient behaviors for various initial conditions (x_0, y_0) near point B, located in the fractal region, is illustrated in Figure 9e. Notably, for $y_0 = 2.2712$, the system exhibits three bursts before ultimately converging to the three-cycle $\mathcal{O}$.

The underlying reason for the noise-induced excitability described above and illustrated in Figure 8 lies in the presence of a fractal region associated with large-amplitude burst transient attractors in the deterministic system (1). For weak noise, random trajectories originating near the cycle $\mathcal{O}$ remain close to its states within the solid part of the short-transient basin (STB), resulting in only minor stochastic fluctuations around the cycle. As the noise intensity increases, these trajectories may cross into the fractal region, triggering large-amplitude burst oscillations. This qualitative shift is anticipated by the positions of the confidence ellipses. In Figure 9b, the ellipse for $\varepsilon = 0.02$ lies entirely within the solid part of the STB. However, the ellipse for $\varepsilon = 0.1$ partially overlaps the "dangerous" fractal zone. This overlap serves as an indicator of the onset of noise-induced excitation. The prediction aligns well with the results of direct numerical simulations (compare Figures 8 and 9b).

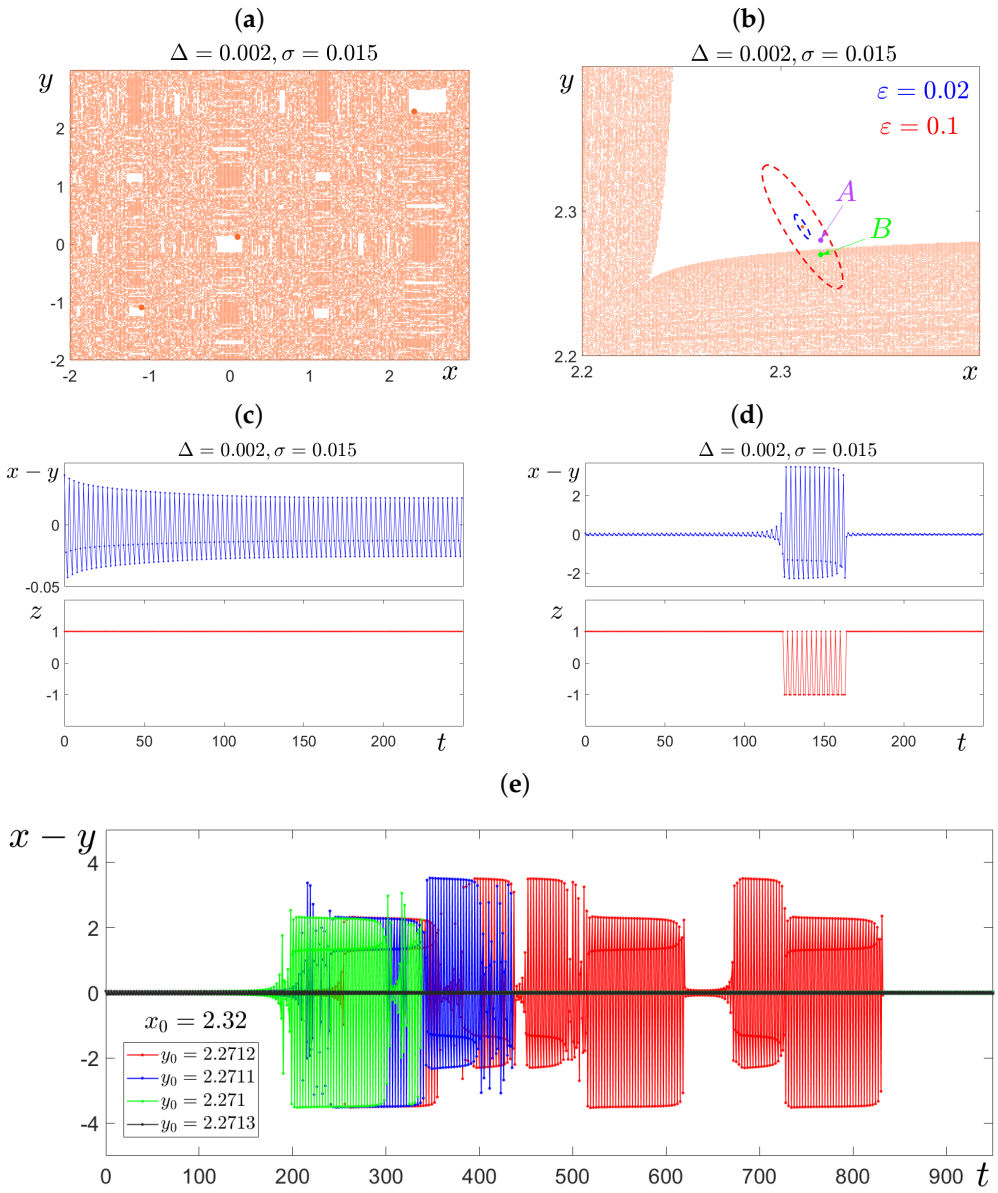


Figure 9. Transient dynamics of the monostable deterministic system (1) with $\gamma = -1.75$, $\Delta = 0.002$, and $\sigma = 0.015$. (**a**) Basin of short transients (white region), where trajectories reach cycle $\mathcal{O}$ within 200 iterations with an accuracy of 0.001. (**b**) Zoomed-in fragment showing confidence ellipses for $\varepsilon = 0.02$ (blue) and $\varepsilon = 0.1$ (red), along with reference points $A(2.32, 2.28)$ and $B(2.32, 2.27)$. (**c**) Time series of $x - y$ (blue) (upper panel) and synchronization indicator z (red) (lower panel) for a trajectory starting at point $A(2.32, 2.28)$. (**d**) Same as in (**c**), but for a trajectory starting at point $B(2.32, 2.27)$. (**e**) Representative examples of transient dynamics for various initial conditions (x_0, y_0).

It is important to note that the distinction between the solid and fractal regions in Figure 9a,b is based on a fixed threshold of $N = 200$ iterations. However, the convergence rate of solutions of system (1) to cycle $\mathcal{O}$ depends on the specific initial condition. This dependence is illustrated in Figure 10, where the color map represents the number of iterations N required to reach the cycle with a convergence accuracy of 0.001. The contrasting characteristics of the solid and fractal regions are clearly visible in this representation. Notably, the confidence ellipse for $\varepsilon = 0.1$ intersects the fractal region, indicating the potential for noise-induced excitation.

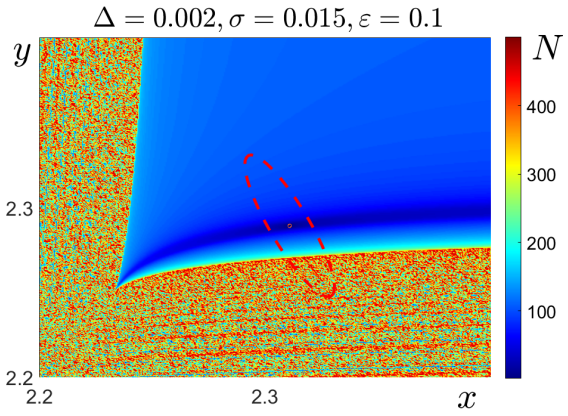


Figure 10. Color map showing the convergence rate of solutions of the monostable deterministic system (1) with $\gamma = -1.75$, $\Delta = 0.002$, and $\sigma = 0.015$ to the three-cycle $\mathcal{O}$. The color indicates the number N of iterations required to achieve a convergence accuracy of 0.001. The red dashed line represents the confidence ellipse for the corresponding stochastic system (2) with noise intensity $\varepsilon = 0.1$.

4.2. Intermittent Synchronization

We now examine how the synchronous behavior of the stochastic system (2) evolves in the excitability regime as the noise intensity increases. Figure 11 presents time series of the variable x and the synchronization indicator z for solutions of the stochastic system (2), initialized at the deterministic three-cycle $\mathcal{O}$. Two noise intensities are considered: $\varepsilon = 0.05$ and $\varepsilon = 0.1$.

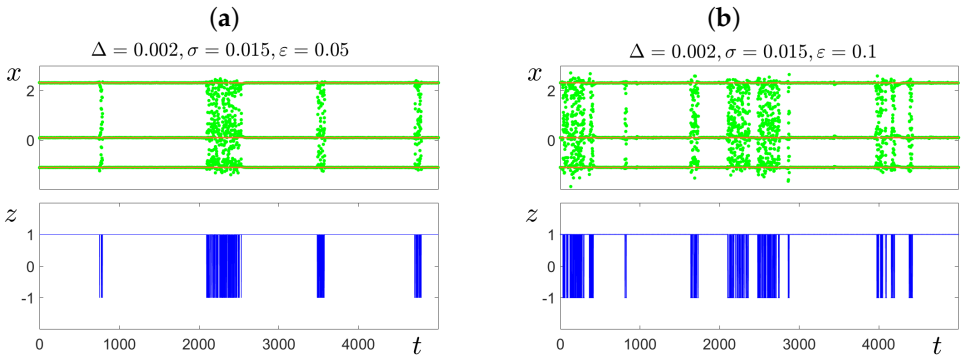


Figure 11. Time series of the x-coordinate (green) and the synchronization indicator z (blue) for solutions of the stochastic system (2), initialized at the deterministic three-cycle $\mathcal{O}$ for noise intensities (**a**) $\varepsilon = 0.05$ and (**b**) $\varepsilon = 0.1$.

The time series reveal two distinct phases: laminar and turbulent. During the laminar phase, the system maintains in-phase synchronization ($z = 1$), with trajectories fluctuating slightly around the points of the periodic three-cycle. In contrast, the turbulent phase is characterized by burst-like oscillations and a breakdown of synchronization. It is important to note that the durations τ of the laminar intervals are random and tend to decrease as the noise intensity increases (compare Figure 11a,b).

Since the turbulent phase emerges due to the presence of noise, this phenomenon belongs to noise-induced intermittency. Similar behavior has been observed in previous studies on systems with randomly modulated parameters [39–44]. Intermittency is typically characterized by the distribution of laminar phase durations, computed for fixed control parameters, and by analyzing the dependence of the mean laminar duration on a critical parameter.

In the statistical analysis, the time series of 10^7 steps was used. Laminar phases were defined as sequences where $z = 1$, and both the mean duration $\langle\tau\rangle$ and the probability $P(\varepsilon)$ were computed based on this threshold.

Figure 12a illustrates the dependence of the mean duration of the laminar phase $\langle\tau\rangle$ on noise intensity ε for different values of the coupling strength σ. For $\sigma = 0.012$, $\sigma = 0.015$, and $\sigma = 0.017$, the deterministic system (1) possesses a single in-phase three-cycle attractor, whereas for $\sigma = 0.02$, the system exhibits a single chaotic attractor. The sharp decline in $\langle\tau\rangle$ for the three-cycle cases marks the onset of noise-induced excitation, characterized by the emergence of temporal bursts. In contrast, the horizontal plateau observed in the chaotic regime suggests that the mean interburst intervals remain unchanged as noise intensity increases.

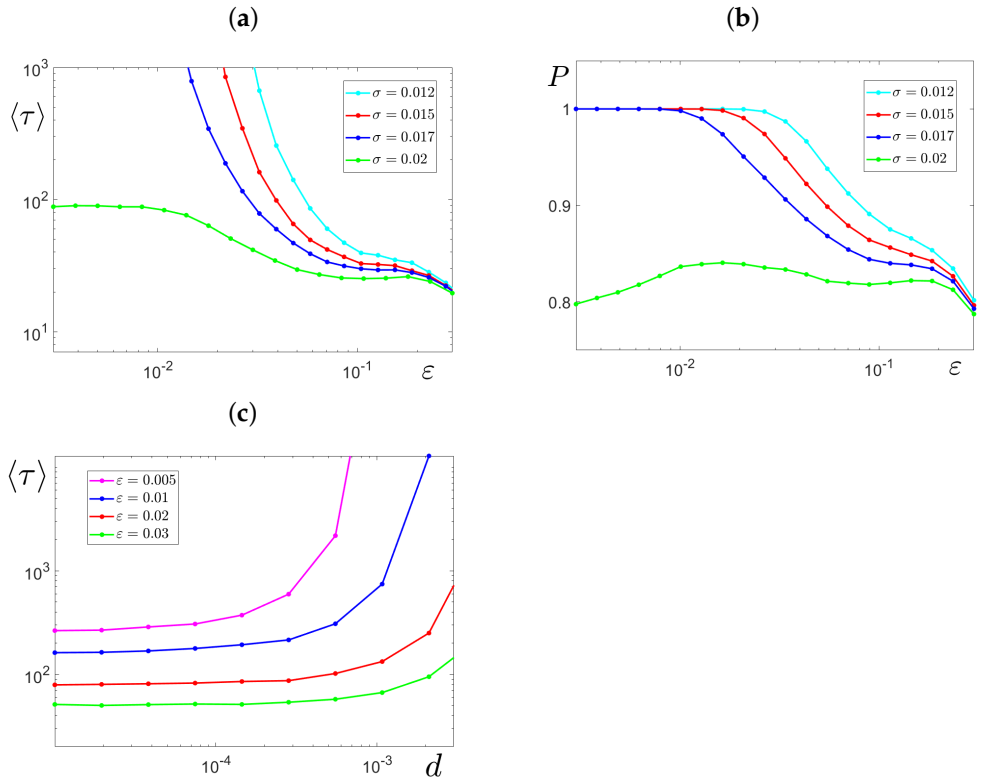


Figure 12. Characteristics of noise-induced intermittency in the stochastic system (2) with $\gamma = -1.75$ and $\Delta = 0.002$. (**a**) Mean duration of laminar phases $\langle\tau\rangle$ corresponding to co-directed behavior ($z = 1$) as a function of noise intensity ε for various coupling strengths σ. (**b**) Probability $P(\varepsilon)$ of observing co-directed behavior as a function of noise intensity for different σ values. (**c**) Mean duration of synchronization intervals $\langle\tau\rangle$ (with $z = 1$) plotted against deviation d of σ from crisis bifurcation point $\sigma_* = 0.019011$, where $\sigma = \sigma_* - d$.

Figure 12b shows the probability of the stochastic system (2) being in the co-directed mode as a function of noise intensity ε for various coupling strengths σ. For all considered values of σ, including the chaotic regime ($\sigma = 0.02$), the system predominantly remains in the co-directed mode, with probabilities $p > 0.5$.

Figure 12c presents the dependence of the mean laminar duration $\langle\tau\rangle$ on the deviation parameter d for different values of ε. As expected, the farther σ is from the crisis bifurcation point σ_*, the longer the mean duration of laminar (co-directed) behavior.

Analysis of the results presented in Figure 12 allows us to conclude that intermittency observed in our study deviates from canonical scaling laws. Classical noise-induced intermittency, typically observed near saddle-node bifurcations, is well known to exhibit universal scaling behavior: the mean laminar phase duration scales with an exponent of

$-1/2$, and the distribution of laminar durations follows a power law with an exponent of $-3/2$ [40–43]. However, as shown in Figure 12, the scaling behavior depends sensitively on both the coupling parameter and the noise intensity. This lack of universality suggests that the intermittency we observe is not simply a textbook example of noise-induced behavior but rather reflects a more complex mechanism tied to the geometry of chaotic transient basins. Moreover, a key distinguishing feature is that, for strong coupling, we observe an increase in the probability of laminar (synchronous) phases with increasing noise intensity in the weak noise regime (see Figure 12 for $\varepsilon = 0.02$), implying a stabilizing role of noise, which contrasts with the typical destabilizing effect seen in many other systems exhibiting noise-induced intermittency.

Finally, in Figure 13, we present the largest Lyapunov exponent Λ, which serves as a key indicator of system stability. This exponent provides a quantitative criterion for distinguishing between regular dynamics ($\Lambda < 0$) and chaotic behavior ($\Lambda > 0$).

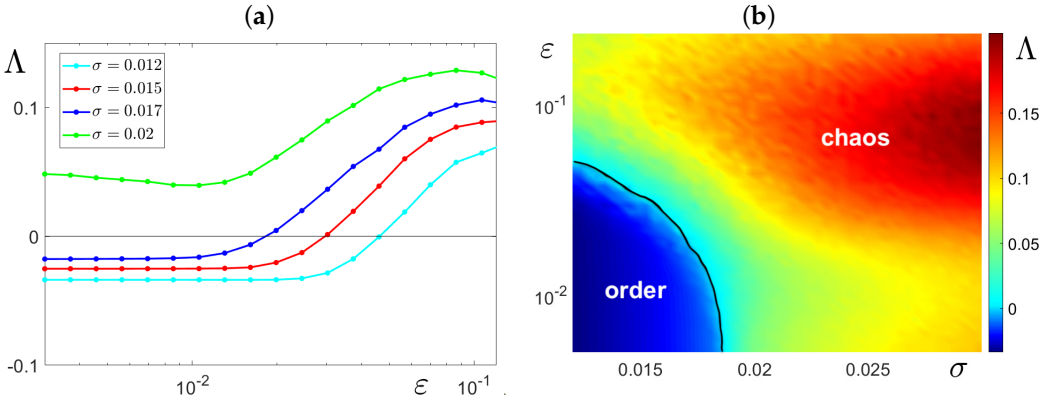


Figure 13. Largest Lyapunov exponent Λ of the stochastic system (2) with $\gamma = -1.75$ and $\Delta = 0.002$. (**a**) Λ as a function of noise intensity ε for different values of the coupling strength σ. (**b**) Two-parameter diagram of Λ in the (σ, ε)-plane showing zones of regular and chaotic dynamics separated by the bifurcation line $\Lambda = 0$.

Figure 13a shows Λ as a function of noise intensity ε for various coupling strengths σ, while Figure 13b illustrates the dependence of Λ on both control parameters, σ and ε. Figure 13b also displays the curve $\Lambda = 0$, which delineates the transition between ordered ($\Lambda < 0$) and chaotic ($\Lambda > 0$) dynamics. The transition is not abrupt but rather gradual, as seen in the plots of $\Lambda(\varepsilon)$ for fixed σ in Figure 13a. From these graphs, one can estimate the threshold noise intensity at which the system transitions from order to chaos. For example, for $\sigma = 0.015$, the Lyapunov exponent crosses zero near $\varepsilon \approx 0.03$, marking the onset of frequent chaotic bursts—consistent with the behavior observed in Figure 8a. This gradual increase in Λ reflects a noise-driven destabilization of regular three-cycles.

5. Conclusions

In this study, we examined the stochastic disruption of synchronization in a system of two non-identical Rulkov neurons coupled via an electrical synapse. Our analysis uncovered regions of mono-, bi-, and tristability, demonstrating how distinct synchronization regimes arise as a function of coupling strength. Through parametric exploration, we identified conditions under which stochastic perturbations to the coupling parameter induce a transition from lag synchronization to monostable in-phase synchronization.

Methodologically, this study combines direct numerical simulations with an analytical framework based on confidence ellipses, providing a powerful tool for identifying and predicting the onset of noise-induced excitations. We extended the confidence domain method, which typically focuses on noise-induced transitions in isolated systems or low-dimensional maps, to a two-parameter space (coupling strength and noise intensity) in a

coupled neural system. This enabled us to map out the boundaries between regimes of regular, intermittent, and chaotic behavior and to link these regions with the geometry of transient basins. These findings advance our understanding of how stochastic effects influence synchronization in coupled neuronal systems and offer valuable insights into noise-driven dynamics in both biological and artificial neural networks.

We demonstrate that noise can induce a transition from a multistable asynchronous regime to a monostable synchronous regime in a network of coupled neurons exhibiting regular (non-chaotic) dynamics in the deterministic limit. To our knowledge, this specific type of noise-induced synchronization through monostabilization has not been reported in previous studies. We identify a novel intermittency regime in which synchronous three-cycles are sporadically interrupted by noise-driven, asynchronous chaotic bursts. This behavior reflects transitions between metastable states and is governed by the underlying structure of chaotic transient basins, a mechanism not previously emphasized in the context of Rulkov models or in the broader literature on stochastic synchronization.

A central finding of this work is the noise-induced intermittency within the synchronous three-cycle regime, where increasing noise intensity leads to transient episodes of desynchronization characterized by chaotic bursts. We showed that this behavior is closely linked to the presence of chaotic transient basins, which act as precursors to the disruption of stable synchronization. Moreover, we identified a specific range of noise intensities where this intermittency persists, with its statistical properties such as laminar phase duration being highly sensitive to the coupling strength. This intermittency differs from previously reported cases in two important ways: (i) it does not follow universal scaling laws, with the scaling behavior varying depending on the coupling strength and noise intensity; and (ii) counterintuitively, weak noise can stabilize laminar dynamics when coupling is strong, resulting in an increased probability of synchronized behavior with increasing noise. These features are closely linked to the presence of chaotic transient basins in the system state space.

Future directions include extending this framework to larger and more complex networks, exploring the role of network topology, and investigating practical implications for neuromorphic engineering and biomedical modeling of brain activity under noisy conditions. While we refrain from making strong claims beyond our scope, these findings suggest that transient-basin-mediated stabilization through weak noise could play a functional role in larger neuronal networks, potentially contributing to noise-enhanced information processing or robustness. This is consistent with previous studies on coherence resonance and perceptual stability in the brain [45,46] and offers a possible direction for future work extending our findings to high-dimensional neural architectures.

Author Contributions: Conceptualization—I.A.B., L.B.R. and A.N.P.; methodology—L.B.R.; software—I.A.B. and I.N.T.; validation—I.A.B. and L.B.R.; formal analysis—I.A.B.; investigation—L.B.R., I.N.T. and A.N.P.; data curation—I.A.B. and L.B.R.; writing—original draft preparation—I.A.B., L.B.R. and A.N.P.; writing—review and editing—I.A.B., L.B.R. and A.N.P.; visualization—I.A.B. and A.N.P.; supervision—L.B.R.; funding acquisition—I.A.B. and L.B.R. All authors have read and agreed to the published version of the manuscript.

Funding: This work was supported by the Russian Science Foundation (N 24-11-00097).

Data Availability Statement: The original contributions presented in this study are included in the article material. Further inquiries can be directed to the corresponding authors.

Conflicts of Interest: The authors declare no conflicts of interest.

References

1. Pikovsky, A.S.; Rosenblum, M.G.; Kurths, J. *Synchronization: A Universal Concept in Nonlinear Sciences*; Cambridge University Press: Cambridge, UK, 2001.
2. Boccaletti, S.; Pisarchik, A.N.; del Genio, C.I.; Amann, A. *Synchronization: From Coupled Systems to Complex Networks*; Cambridge University Press: Cambridge, UK, 2018.
3. Ghosh, D.; Frasca, M.; Rizzo, A.; Majhi, S.; Rakshit, S.; Alfaro-Bittner, K.; Boccaletti, S. The synchronized dynamics of time-varying networks. *Phys. Rep.* **2022**, *949*, 1–63. [CrossRef]
4. Wu, X.; Wu, X.; Wang, C.Y.; Mao, B.; Lu, J.; Lü, J.; Zhang, Y.C.; Lü, L. Synchronization in multiplex networks. *Phys. Rep.* **2024**, *1060*, 1–54. [CrossRef]
5. Uhlhaas, P.J.; Singer, W. Neural synchrony in brain disorders: Relevance for cognitive dysfunctions and pathophysiology. *Neuron* **2006**, *52*, 155–168. [CrossRef] [PubMed]
6. Jiruska, P.; de Curtis, M.; Jefferys, J.G.; Schevon, C.A.; Schiff, S.J.; Schindler, K. Synchronization and desynchronization in epilepsy: Controversies and hypotheses. *J. Physiol.* **2013**, *591*, 787–797. [CrossRef]
7. Popovych, O.V.; Tass, P.A. Control of abnormal synchronization in neurological disorders. *Front. Neurol.* **2014**, *5*, 268. [CrossRef] [PubMed]
8. Destexhe, A.; Rudolph-Lilith, M. *Neuronal Noise*; Springer Series in Computational Neuroscience; Springer: New York, NY, USA, 2012; Volume 8.
9. Kelly, F.; Yudovina, E. *Stochastic Networks*; Cambridge University Press: Cambridge, UK, 2014; Volume 2.
10. Kulkarni, A.; Ranft, J.; Hakim, V. Synchronization, stochasticity, and phase waves in neuronal networks with spatially-structured connectivity. *Front. Comput. Neurosci.* **2020**, *14*, 569644. [CrossRef]
11. Olin-Ammentorp, W.; Beckmann, K.; Schuman, C.D.; Plank, J.S.; Cady, N.C. Stochasticity and robustness in spiking neural networks. *Neurocomputing* **2021**, *419*, 23–36. [CrossRef]
12. Park, C.; Rubchinsky, L.L. Intermittent synchronization in a network of bursting neurons. *Chaos* **2011**, *21*, 033125. [CrossRef]
13. Berger, A.; Qian, H.; Wang, S.; Yi, Y. Intermittent synchronization in finite-state random networks under Markov perturbations. *Commun. Math. Phys.* **2021**, *384*, 1945–1970. [CrossRef]
14. Simiu, E. *Chaotic Transitions in Deterministic and Stochastic Dynamical Systems: Applications of Melnikov Processes in Engineering, Physics, and Neuroscience*; Princeton University Press: Princeton, NJ, USA, 2002.
15. Kurrer, C.; Schulten, K. Noise-induced synchronous neural oscillations. *Phys. Rev. E* **2002**, *51*, 6213–6218. [CrossRef]
16. Zhou, H.; Liu, Z.; Li, W. Sampled-data intermittent synchronization of complex-valued complex network with actuator saturations. *Nonlin. Dyn.* **2022**, *107*, 1023–1047. [CrossRef]
17. Kraut, S.; Feudel, U.; Grebogi, C. Preference of attractors in noisy multistable systems. *Phys. Rev. E* **1999**, *59*, 5253–5260. [CrossRef] [PubMed]
18. Kraut, S.; Feudel, U. Multistability, noise, and attractor hopping: The crucial role of chaotic saddles. *Phys. Rev. E* **2002**, *66*, 015207. [CrossRef]
19. Koronovskii, A.A.; Hramov, A.E.; Grubov, V.V.; Moskalenko, O.I.; Sitnikova, E.; Pavlov, A.N. Coexistence of intermittencies in the neuronal network of the epileptic brain. *Phys. Rev. E* **2016**, *93*, 032220. [CrossRef] [PubMed]
20. Pisarchik, A.N.; Hramov, A.E. *Multistability in Physical and Living Systems: Characterization and Applications*; Springer: Cham, Switzerland, 2022.
21. Rulkov, N.F. Regularization of synchronized chaotic bursts. *Phys. Rev. Lett.* **2001**, *86*, 183–186. [CrossRef]
22. Wang, C.; Cao, H. Stability and chaos of Rulkov map-based neuron network with electrical synapse. *Commun. Nonlin. Sci. Numer. Simul.* **2015**, *20*, 536–545. [CrossRef]
23. Dijkstra, K.; Kuznetsov, Y.A.; van Putten, M.J.A.M.; van Gils, S.A. A rate-reduced neuron model for complex spiking behavior. *J. Math. Neurosci.* **2017**, *11*, 13. [CrossRef]
24. Ge, P.; Cao, H. Chaos in the Rulkov neuron model based on Marotto's theorem. *Internat. J. Bifurc. Chaos* **2021**, *31*, 2150233. [CrossRef]
25. Wang, Y.; Zhang, X.; Liang, S. New phenomena in Rulkov map based on Poincaré cross section. *Nonlin. Dyn.* **2023**, *111*, 19447–19458. [CrossRef]
26. López, J.; Coccolo, M.; Capeáns, R.; Sanjuán, M.A.F. Controlling the bursting size in the two-dimensional Rulkov model. *Commun. Nonlin. Sci. Numer. Simul.* **2023**, *120*, 107184. [CrossRef]
27. Li, G.; Duan, J.; Yue, Z.; Li, Z.; Li, D. Dynamical analysis of the Rulkov model with quasiperiodic forcing. *Chaos Solitons Fractals* **2024**, *189*, 115605. [CrossRef]
28. Marghoti, G.; Ferrari, F.A.S.; Viana, R.L.; Lopes, S.R.; Prado, T.d.L. Coupling dependence on chaos synchronization process in a network of Rulkov neurons. *Intern. J. Bifurc. Chaos* **2023**, *33*, 2350132. [CrossRef]
29. Ge, P.; Cheng, L.; Cao, H. Complete synchronization of three-layer Rulkov neuron network coupled by electrical and chemical synapses. *Chaos* **2024**, *34*, 043127. [CrossRef]

30. Le, B.B. Asymmetric coupling of nonchaotic Rulkov neurons: Fractal attractors, quasimultistability, and final state sensitivity. *Phys. Rev. E* **2025**, *111*, 034201. [CrossRef] [PubMed]
31. Bashkirtseva, I.; Ryashko, L. Stochastic sensitivity analysis of noise-induced phenomena in discrete systems. In *Recent Trends in Chaotic, Nonlinear and Complex Dynamics*; World Scientific Series on Nonlinear Science Series B; World Scientific: Singapore, 2021; Chapter 8, pp. 173–192.
32. Garain, K.; Sarathi Mandal, P. Stochastic sensitivity analysis and early warning signals of critical transitions in a tri-stable prey-predator system with noise. *Chaos* **2022**, *32*, 033115. [CrossRef]
33. Guo, K.; Jiang, J. Stochastic sensitivity analysis of periodic attractors in non-autonomous nonlinear dynamical systems based on stroboscopic map. *Phys. Lett. A* **2014**, *378*, 2518–2523. [CrossRef]
34. Xu, C.; Yuan, S.; Zhang, T. Stochastic sensitivity analysis for a competitive turbidostat model with inhibitory nutrients. *Int. J. Bifurcat. Chaos* **2016**, *26*, 1650173. [CrossRef]
35. Sun, Y.; Hong, L.; Jiang, J. Stochastic sensitivity analysis of nonautonomous nonlinear systems subjected to Poisson white noise. *Chaos Solitons Fractals* **2017**, *104*, 508–515. [CrossRef]
36. Xu, C.; Yuan, S.; Zhang, T. Confidence domain in the stochastic competition chemostat model with feedback control. *Appl. Math. J. Chinese Univ.* **2018**, *33*, 379–389. [CrossRef]
37. Chen, J.; Zhang, T.; Zhou, Y. Stochastic sensitivity and dynamical complexity of newsvendor models subject to trade credit. *Math. Comput. Simul.* **2021**, *181*, 471–486. [CrossRef]
38. Bashkirtseva, I.A.; Ryashko, L.B.; Pisarchik, A.N. Dragon intermittency at the transition to synchronization in coupled Rulkov neurons. *Mathematics* **2025**, *13*, 415. [CrossRef]
39. Stone, E.; Holmes, P. Noise-induced intermittency in a model of turbulent boundary layer. *Phys. D* **1989**, *37*, 20–32. [CrossRef]
40. Manneville, P.; Pomeau, Y. Intermittency and the Lorenz model. *Phys. Lett.* **1979**, *75A*, 1–2. [CrossRef]
41. Platt, N.; Hammel, S.M.; Heagy, J.F. Effects of additive noise on on-off intermittency. *Phys. Rev. Lett.* **1994**, *72*, 3498. [CrossRef] [PubMed]
42. Heagy, J.F.; Platt, N.; S M Hammel, S.M. Characterization of on-off intermittency. *Phys. Rev. E* **1994**, *48*, 1140. [CrossRef]
43. Fujisaka, H.; Ouchi, K.; Ohara, H. On-off convection: Noise-induced intermittency near the convection threshold. *Phys. Rev. E* **2001**, *64*, 036201. [CrossRef]
44. Moskalenko, O.; Koronovskii, A.A.; Zhuravlev, M.O.; Hramov, A.E. Characteristics of noise-induced intermittency. *Chaos Solitons Fractals* **2018**, *117*, 269–275. [CrossRef]
45. Simonotto, E.; Riani, M.; Seife, C.; Roberts, M.; Twitty, J.; Moss, F. Visual perception of stochastic resonance. *Phys. Rev. Lett.* **1997**, *78*, 1186–1189. [CrossRef]
46. Pisarchik, A.N.; Hramov, A.E. Coherence resonance in neural networks: Theory and experiments. *Phys. Rep.* **2023**, *1000*, 1–57. [CrossRef]

Disclaimer/Publisher's Note: The statements, opinions and data contained in all publications are solely those of the individual author(s) and contributor(s) and not of MDPI and/or the editor(s). MDPI and/or the editor(s) disclaim responsibility for any injury to people or property resulting from any ideas, methods, instructions or products referred to in the content.